Asymmetric Switching of Edge Modes by Dynamically Encircling Multiple Exceptional Points

Yicong Zhang,[1] Weiwei Liu,[1,2,*] Shuaifei Ren,[1] Tianyan Chai,[1] Yanan Wang,[1] Hua Long,[1] Kai Wang,[1] Bing Wang,[1,†] and Peixiang Lu[1,2]

[1] *Wuhan National Laboratory for Optoelectronics and School of Physics, Huazhong University of Science and Technology, Wuhan 430074, China*

[2] *Hubei Key Laboratory of Optical Information and Pattern Recognition, Wuhan Institute of Technology, Wuhan 430205, China*

(Received 24 January 2023; accepted 12 May 2023; published 15 June 2023)

Dynamically encircling exceptional points (EPs) in the parameter space of a non-Hermitian system has drawn widespread attention for realizing asymmetric mode switching and related applications. While previous works have been restricted to two-level systems, the switching between edge states in a multistate system that contains more complex dynamics remains to be explored. Herein, asymmetric switching of edge modes in multistate systems is demonstrated by encircling multiple EPs. A multistate non-Hermitian system containing multiple EPs is constructed based on a one-dimensional lattice, which can support four edge-localized modes. Dynamically encircling the EPs in parameter space leads to a specific edge mode surviving to the end, determined by the encircling direction. Correspondingly, optical waveguide arrays are designed to investigate mode evolution through refractive index modulation. Simulated results show that clockwise (counterclockwise) encirclement leads to an output mode localized at the left (right) side of the waveguide array with a phase difference of 0 (π), regardless of the input modes; this excellently illustrates the asymmetric switching of edge modes in a multistate system. Moreover, such an effect can be extended to the multistate system with an arbitrary number of EPs. This work enables investigation of interesting effects in non-Hermitian physics by engineering the EPs and topological properties, especially for complex multistate systems, which will be useful for developing functional nanophotonic devices.

DOI: 10.1103/PhysRevApplied.19.064050

I. INTRODUCTION

Exceptional points (EPs), which represent the peculiar singularities in non-Hermitian systems [1–5], have aroused widespread attention in recent years. Differing from the degeneracies in the parameter space of Hermitian systems, the eigenvalues and the corresponding eigenvectors coalesce simultaneously at the EPs of non-Hermitian systems. This unique characteristic contributes to the distinctive topology of energy surfaces of non-Hermitian systems and gives rise to phenomena that are drastically distinct from those in the Hermitian realm [6,7]. Up to now, a series of novel effects and practical functions in optics have been achieved utilizing EPs, such as light stopping [8], electromagnetically induced transparency [9,10], coherent perfect absorption [11–14], unidirectional reflectionless light propagation [15–19], ultrasensitive sensing [20–25], loss-induced revival of lasing [26–29], topological amplification [30], and symmetry-protected topological lasers [31]. In particular, mode switching induced by dynamically encircling the EP in parameter space has had significant impact in optical physics and devices. When adiabatically encircling the EP in parameter space, the initial eigenstate will transfer to another with an additional geometric phase. Owing to the topological features of the Riemann surface and the nonadiabatic transitions (NATs), the process exhibits asymmetric mode switching in which the output mode is determined by the direction of the parameter loop rather than the input [3,4,32–37].

Up to now, asymmetric mode switching has been explored in optical waveguides [38–41], coupled microresonators [42–44], and photonic crystals [45,46]. However, most of the previous studies are restricted to systems supporting only two eigenstates, and the mode switching happens between the counterparts. For multistate systems, the energy surfaces possess more complex topological structures. Therefore, the dynamical evolutions of the states are also more complicated [47–49]. Specifically, since multiple EPs can form in the parameter space of a multistate system, dynamically encircling the EPs will lead to richer mode-switching behaviors with new physical

*lwhust@hust.edu.cn
†wangbing@hust.edu.cn

mechanisms and applications. More recently, Yu *et al.* [50] studied the dynamical encircling of an arbitrary number of EPs in a periodic waveguide array. The mode switching in the multistate non-Hermitian system was governed by a general rule with outcomes located at the Brillouin-zone boundary. As the reported waveguide array can only support bulk modes, asymmetric switching of edge states in the multistate system remains to be explored, and this will allow investigation of further rich topological and dynamic properties in multistate non-Hermitian systems.

In this work, we demonstrate an asymmetric switching of edge modes in a multistate non-Hermitian system by dynamically encircling multiple EPs. A one-dimensional (1D) lattice model is proposed to act as a multistate non-Hermitian system, which can support four edge modes distinguished with intensity and phase distribution of the eigenstates. Since multiple EPs exist in the parameter space of the non-Hermitian system, asymmetric switching between the edge modes is achieved by encircling the EPs adiabatically. Correspondingly, planar optical waveguide arrays are designed with refractive index modulation. The mode evolutions in the optical waveguide arrays are simulated, indicating that the asymmetric switching of edge modes can be realized in optics and extended to multistate systems with an arbitrary number of EPs.

II. ONE-DIMENSIONAL LATTICE MODEL AND EDGE STATES

Firstly, a 1D lattice model with open boundaries is proposed to support edge states, as shown schematically in Fig. 1(a). The lattice chain is composed of trimers (marked by orange boxes) and link sites, in which the lattice sites are defined as A, B, C, and B in sequence. Corresponding on-site energy terms for sites A, B, and C are $\alpha+\delta$, α, and $\alpha-\delta$, respectively. Utilizing the tight-binding model [51,52], the intersite coupling strength in each trimer is set as κ_1, while that between the link sites B and adjacent sites A or C is κ_2. Considering that link sites B emerge on both ends of the chain, the truncated chain possesses $4N+1$ sites, with N marking the number of trimers.

Figures 1(b) and 1(c) show energy band diagrams of the truncated structure as δ varies, with $\kappa_1=4\kappa_2=4\kappa$ and $\kappa_2=4\kappa_1=4\kappa$, respectively ($\alpha=0$ for simplicity). In the former case, all of the $4N+1$ bands represent bulk eigenmodes of the lattice, which are separated into three groups by two gaps, while for the latter case, four bands

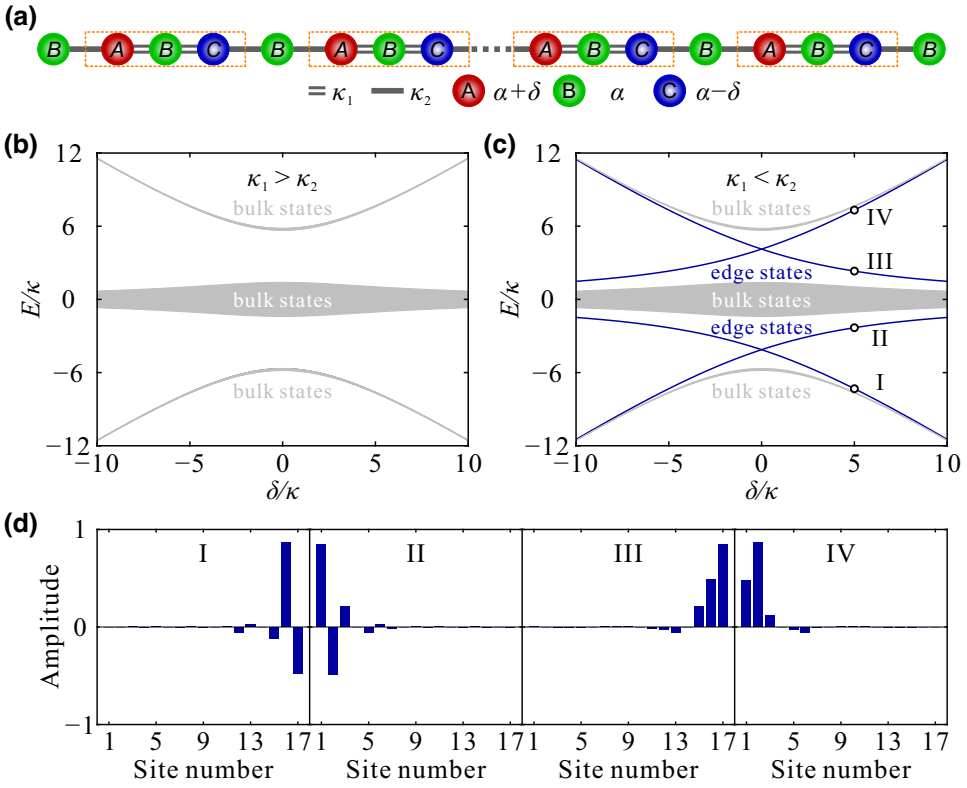

FIG. 1. (a) Scheme of the truncated 1D lattice model and the defined trimers are marked with the orange boxes. (b),(c) Energy spectra for the 1D lattice with open boundary condition for $\kappa_1=4\kappa_2$ and $\kappa_2=4\kappa_1$, respectively. The gray bands represent the bulk states while the blue bands represent the edge states. (d) Distributions of the eigenstates at points I–IV in (c), respectively, with the number of trimers $N=4$.

corresponding to the edge states arise in the gaps, representing the existence of the eigenmodes localized at the boundary of the chain. As the chain possesses an asymmetric distribution with respect to the central site for $\delta \neq 0$, the edge modes distribute asymmetrically at two sides of the chain. Figure 1(d) depicts distributions of the four edge modes at $\delta = 5\kappa$ ($N = 4$, for example), which shows that modes I and III are localized at the right side and modes II and IV are localized at the left side. Moreover, the phase differences between adjacent sites of each mode are different. The phase difference between adjacent sites for edge modes I and II is π, while it is 0 for edge modes III and IV. As analyzed above, the edge modes of the 1D lattice chain are characterized not only by the intensity distribution but also by the phase. Therefore, this 1D lattice chain demonstrates a potential model for realizing switching between the edge-localized modes with inverted phase differences.

III. EXCEPTIONAL POINTS AND ENCIRCLING LOOP IN PARAMETER SPACE

Typical two-level parity-time (PT) symmetric systems can be described by the Hamiltonian matrix [2,4,53]

$$H_{\mathrm{PT}} = \begin{bmatrix} \alpha + i\gamma & \kappa \\ \kappa & \alpha - i\gamma \end{bmatrix}, \tag{1}$$

where the real parts of the on-site energy terms are equal while the imaginary parts are inverted. The positions of EPs depend on gain or loss (γ) and coupling coefficient (κ). Inspired by this basic model, the corresponding non-Hermitian counterpart of the 1D lattice model can be constructed by adding opposite imaginary parts to the on-site energy terms of sites A and C. The non-Hermitian Hamiltonian can be written as

$$H = \begin{bmatrix} \alpha & \kappa_2 & & & & & & & \\ \kappa_2 & \alpha + \delta + i\gamma & \kappa_1 & & & & & & \\ & \kappa_1 & \alpha & \kappa_1 & & & & & \\ & & \kappa_1 & \ddots & \ddots & & & & \\ & & & \ddots & \ddots & \kappa_1 & & & \\ & & & & \kappa_1 & \alpha & & \kappa_1 & \\ & & & & & \kappa_1 & \alpha - \delta - i\gamma & \kappa_2 & \\ & & & & & & \kappa_2 & \alpha & \end{bmatrix}, \tag{2}$$

which suggests that EPs arise at $\delta = 0$. Figures 2(a) and 2(b) plot the real and imaginary parts of the eigenvalues ($\kappa_1 = 6 \times 10^{-4}$, $\kappa_2 = 2.6 \times 10^{-3}$, $\alpha = 0$) with $\gamma < 0$ and $\gamma > 0$, respectively, for a better view, and the surfaces exhibit symmetric distribution on both sides of $\gamma = 0$. For clarity, the eigenvalue surfaces of the bulk states and edge states are marked by gray and black frames, respectively. For this multistate system, there exist multiple second-order EPs lying on the line $\delta = 0$. The number of EPs increases with the number of trimers (N) and two exceptional lines (ELs) with two isolated EPs are formed when N tends toward infinity [Fig. 2(c)]. Interestingly, the range of γ_{EP} is invariable regardless of N, which indicates that a parameter loop can be designed to encircle all the EPs of the multistate systems with arbitrary N for realizing asymmetric switching of the edge states.

For waveguide arrays based on the lattice model shown in Fig. 1(a), each site can be regarded as an individual waveguide and the on-site energy terms in Eq. (2) correspond to the propagation constants. For convenience, the parameters in Eq. (2) are normalized to $k_0 = 2\pi/\lambda_0$, where λ_0 represents the wavelength in vacuum [i.e., α and δ represent the real parts while γ represents the imaginary parts of effective mode indices in Eq. (2)]. Assuming that the light propagates in the waveguide along the z axis, spatial modulation along the propagation direction is utilized for realizing mode switching by encircling the EPs in the parameter space. To achieve the encircling loop, the Start/End point in (γ, δ) space is set at $\gamma = 0$ and $\delta = 5 \times 10^{-3}$, corresponding to the Hermitian model in Fig. 1(a). The parameter loop is designed as functions of the coordinate z,

$$\gamma = \Delta\gamma \sin(2\pi z/L), \tag{3}$$

$$\delta = \delta_0 - \Delta\delta \sin(\pi z/L), \tag{4}$$

where δ_0, $\Delta\gamma$, and $\Delta\delta$ are respectively set as 5×10^{-3}, 6×10^{-3}, and 7.5×10^{-3} to make sure that all the EPs ($\gamma_{\mathrm{EP\ min}} = -5.33 \times 10^{-3}$, $\gamma_{\mathrm{EP\ max}} = 5.33 \times 10^{-3}$) can be encircled in the loop, and L represents the length of evolution period. Figure 2(d) plots the waterdrop-shaped parameter loop encircling the EPs. At the Start/End point, four edge modes are distributed similarly to those in Fig. 1(d). The state of the system during the evolution can be regarded as the weighted superposition of all instantaneous eigenmodes. The quantum adiabatic approximation and breakdown of the adiabatic theorem in the presence of loss and gain indicate that the system tends to evolve to the stable mode with the lowest relative loss (or the largest gain) when parameters adiabatically encircle the EPs [34,54–56]. Simultaneously, the unique topological property of the Riemann surface in the vicinity of the EPs reveals that opposite encircling directions can result in different tendencies of mode evolution, representing an asymmetric mode switching. For a multistate system, the dynamics of encircling an arbitrary number of EPs can be analyzed by treating the multiple EPs as a whole [50].

To facilitate the analysis of the mode evolution process and predict the tendency of mode switching, the highest-gain modes are marked in different areas of (γ, δ) space, as shown in Fig. 3(a). The designed parameter loop is plotted with a white curve. The (γ, δ) space is divided into six regions: the four colored ones correspond to the highest-gain edge modes and the gray regions represent the

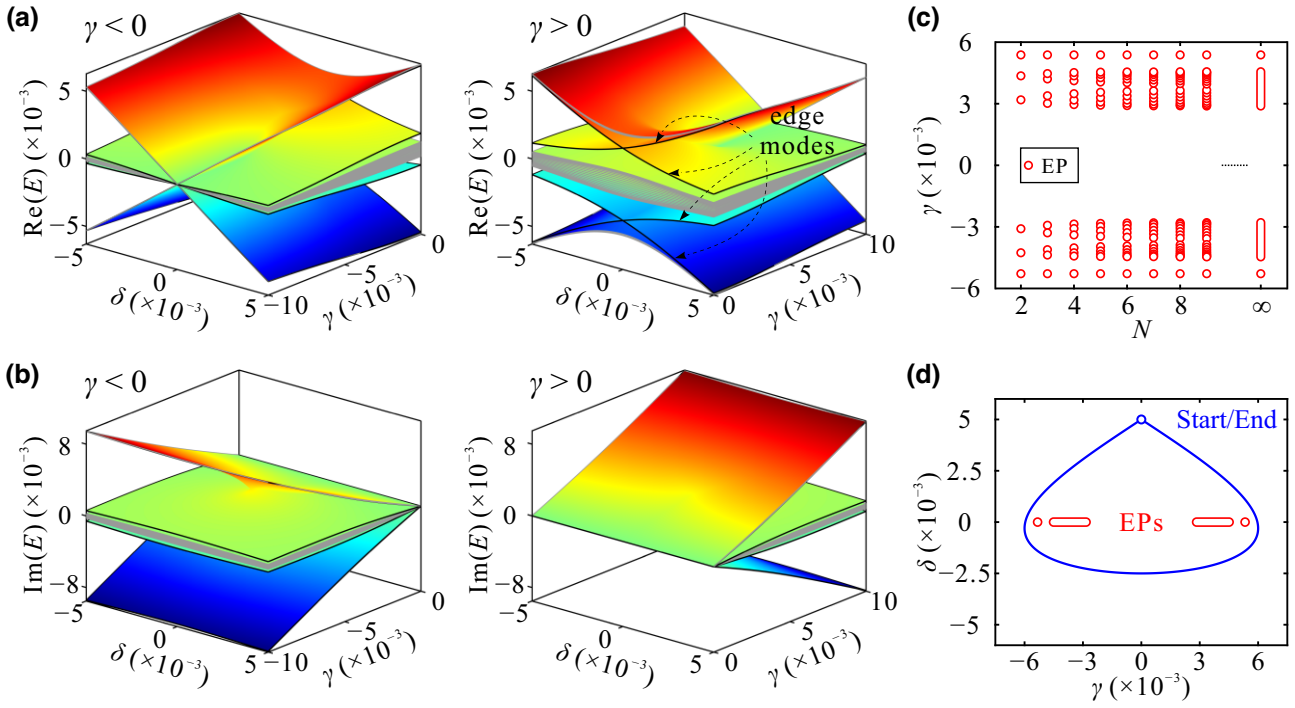

FIG. 2. (a) Real and (b) imaginary parts of the eigenvalues in (γ, δ) space with $\gamma < 0$ and $\gamma > 0$, respectively. The eigenvalue surfaces for the bulk and edge states are distinguished by the gray and black frames, respectively. (c) Positions of the EPs with different numbers of periods. As N tends to infinity, two isolated EPs and two ELs can be observed. (d) The designed parameter loop that encircles all the EPs.

bulk modes. For $N = 4$, distributions of the highest-gain edge modes are plotted in the insets of the corresponding regions. When the system parameters change slowly enough, NATs occur due to a breakdown of the adiabatic theorem when the weight of the highest-gain mode in the mixed state is lower than those of other modes. As a result, the weight of the highest-gain mode increases and gradually dominates in the system [34]. If an arbitrary edge mode acts as the initial state of the system, multiple NATs occur in the whole encircling process. However, the final dominant mode depends on the last NAT. As the Start/End point of the loop is located on the boundary between the blue and red regions, the clockwise (CW) and counterclockwise (CCW) encirclements make the parameters approach the destination from the red and blue sides, respectively. Therefore, we can predict that the CW and CCW encirclements will lead to edge modes IV and I as the dominant output modes respectively.

The evolution of eigenvalues along the parameter loop is plotted in Figs. 3(b) and 3(c). For the CW encirclement corresponding to evolving from $z = 0$ to $z = L$, the imaginary parts of the eigenvalues for edge modes I and III are negative (gain) while those for edge modes II and IV are positive (loss) before the middle of the evolution process. After that, the signs of the imaginary parts of all these four eigenvalues reverse, thus modes II and IV become the gain modes. In the case of the CCW encirclement, opposite results can be obtained as the evolution direction is reversed. For further demonstration on the NAT-related asymmetric mode switching, we calculate the evolution of the amplitudes of all eigenmodes by solving the coupled mode equations for $N = 2$ (see Sec. A in the Supplemental Material [57]). The calculation results indicate that, as the encircling loop is about to reach the end, the amplitude of the highest-gain mode is always much larger than all the other modes, regardless of the initial edge modes. As depicted by the red and blue arrows in Fig. 3(c), the corresponding edge modes IV and I become dominant in the final state of the evolution for propagation along $+z$ and $-z$ directions, respectively, which verifies the prediction above. The chiral dynamics induced by encircling the EPs is irrelevant to the term α in Eq. (2), as the value of α only shifts the energy surfaces while the topological properties are completely unaffected.

IV. ASYMMETRIC SWITCHING OF EDGE MODES IN OPTICAL WAVEGUIDE ARRAYS

In this section, we demonstrate the asymmetric switching of edge modes utilizing 2D slab waveguide arrays. As illustrated in Fig. 4(a), the waveguide array is composed of three types of waveguides with different modulations of refractive indices, which are marked with red, green, and blue, respectively. Light propagates in the waveguides

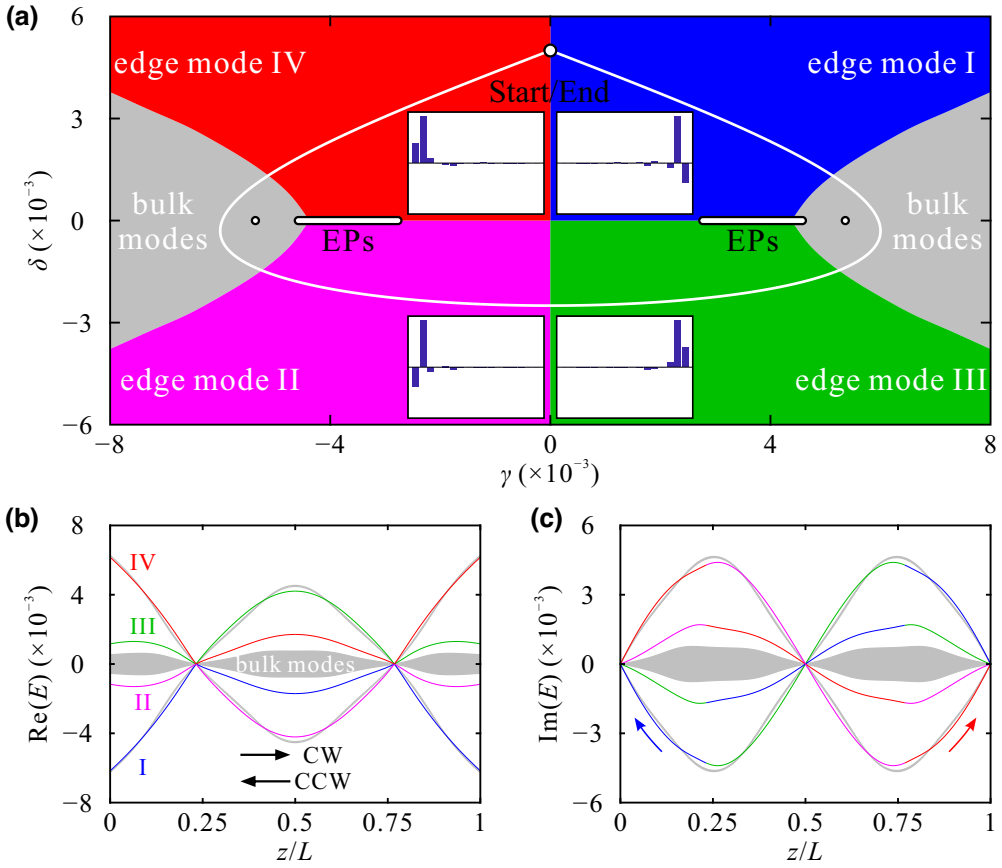

FIG. 3. (a) The mode with the highest gain (i.e., the corresponding eigenvalue with the smallest imaginary part) in (γ, δ) space. (b) Real and (c) imaginary parts of the eigenvalues as δ and γ evolve along the trajectory shown in (a). Eigenvalues of the bulk states are plotted in gray and those of the four edge states are plotted in blue, magenta, green, and red. The black arrows in (b) indicate the correlation between the encircling directions and evolution of z. The red and blue arrows in (c) mark the edge modes with the lowest imaginary parts of the eigenvalues (i.e., the highest gain) when z is about to reach both ends.

along the z axis. The waveguide array can be described by a coupled mode equation

$$-i\frac{d}{dz}\begin{bmatrix} a_1(z) \\ a_2(z) \\ \vdots \\ a_{4N}(z) \\ a_{4N+1}(z) \end{bmatrix} = k_0 H \begin{bmatrix} a_1(z) \\ a_2(z) \\ \vdots \\ a_{4N}(z) \\ a_{4N+1}(z) \end{bmatrix}, \qquad (5)$$

where k_0 is the propagation constant in free space and $a_m(z)$ stands for the complex mode amplitude in the mth waveguide [58,59]. The Hamiltonian matrix H is given in Eq. (2), in which δ and γ vary with z, and the term α represents the effective mode index of the unmodulated waveguides.

In the simulations, the operating wavelength is set at $\lambda_0 = 1550$ nm (i.e., $k_0 = 4.0537\ \mu\text{m}^{-1}$) and the widths of all the slab waveguides are set as $w = 800$ nm. The refractive indices of the background and waveguides A, B, and C are respectively defined as $n_0 = 1.7$, $n_A(z) = 2.0055 - 0.0083\sin(\pi z/L) + i[0.0066\sin(2\pi z/L)]$, $n_B = 2$, $n_C(z) = 1.9945 + 0.0083\sin(\pi z/L) - i[0.0066\sin(2\pi z/L)]$, which ensures that the parameter loop is constructed as designed previously. Figure 4(b) plots the modulation functions of the real and imaginary parts of n_A and n_C. To fulfill the requirement of constant coupling strengths $\kappa_1 = 6 \times 10^{-4}$ and $\kappa_2 = 2.6 \times 10^{-3}$, the gaps between intracell and intercell adjacent waveguides are set as $g_{AB1} = 1265$ nm, $g_{BC1} = 1275$ nm, $g_{AB2} = 850$ nm, and $g_{BC2} = 860$ nm. The perturbation on the coupling strength caused by varying refractive indices of waveguides is far less than κ_1 and κ_2, indicating that κ_1 and κ_2 can be regarded as constants (see Sec. C in the Supplemental Material [57] for details). In addition, the next-nearest-neighbor coupling is below 10^{-4}, which is negligible and the tight-binding model is well satisfied.

Effective mode indices and distribution of eigenmodes of the slab waveguide arrays at terminals are calculated using COMSOL Multiphysics. For $N = 2$, 3, and 4, the effective mode indices and corresponding distributions of E_y for four edge modes are shown in Figs. 4(c)–4(e), respectively. The numerically calculated effective mode indices are in good agreement with the theoretical results [Fig. 1(c)] for

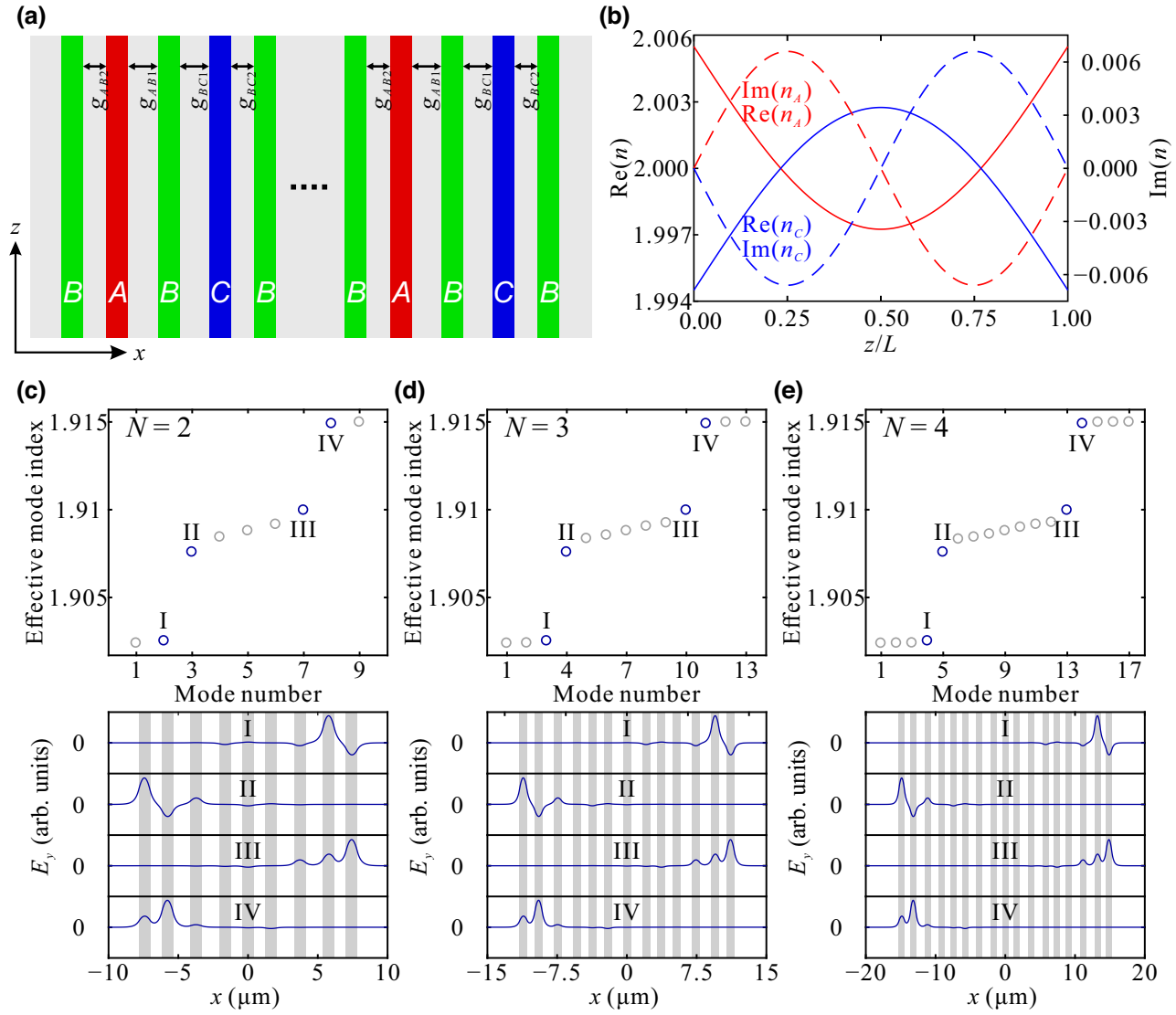

FIG. 4. (a) Scheme of the planar waveguide array designed based on the truncated lattice model. The waveguides are arranged along the x axis, and the light propagates along the z direction. Waveguides A, B, and C are shown in red, green, and blue, respectively. (b) Modulation functions for complex refractive indices of waveguides A and C. (c)–(e) Calculated effective mode indices for the eigenmodes of waveguide arrays with $N = 2$, 3, and 4, respectively. Distributions of E_y components of four edge modes are also shown below. The corresponding positions of the waveguides are marked with the gray bars.

both bulk modes and edge modes. E_y profiles along the x axis for edge modes I–IV also fit well with the eigenstates in Fig. 1(d), indicating that the slab waveguide array can be well described using the proposed 1D lattice model. Moreover, for an arbitrary number of unit cells, the slab waveguide array is still able to support the desired edge modes at both boundaries.

To guarantee that the parameters vary sufficiently slowly along the z axis for adiabatic evolution and high efficiency of mode switching [39,40,60], the length of the waveguide array for $N = 2$ is set as 2500 μm. Figure 5 presents the distribution of electric field amplitude ($|\boldsymbol{E}|$) in the waveguide array and the corresponding E_y component at input and output terminals. The power is normalized in the propagation direction to clearly reveal the mode-transfer process. For each edge mode, the amplitudes in the three waveguides closest to the boundary of the array are much larger than the rest. Therefore, we focus only on the field in these waveguides to identify the edge modes at the output terminal. For incident edge modes I–IV at $z = 0$ (CW encirclement), as displayed in Fig. 5(a), the output is dominantly occupied by the mode localized at the left side of the waveguide array. In addition, the E_y components of the output edge modes display a phase difference of zero at the three left-most waveguides for all four situations. This indicates that incident edge modes can be switched

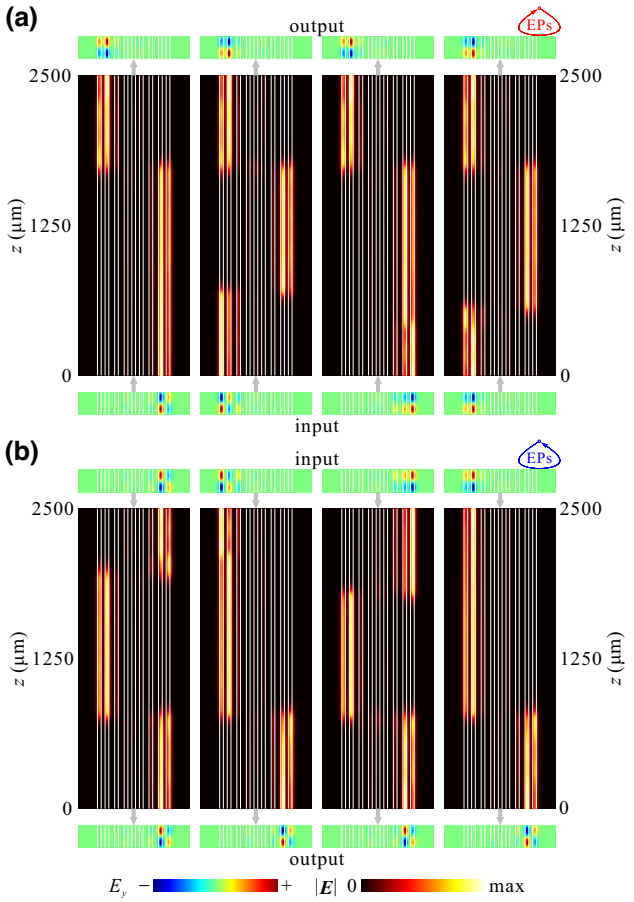

FIG. 5. Numerically simulated electric field profiles with edge modes injected at (a) $z = 0$ and (b) $z = 2500$ μm for the waveguide array with $N = 2$. The distributions of the E_y component at both terminals with the length of 0.8 μm are also shown. The corresponding encircling directions in (γ, δ) space for both propagation directions are marked by the arrows at the top right corner.

to mode IV, regardless of the input modes. In contrast, for incidence at $z = L$ [CCW encirclement, Fig. 5(b)], the output is dominantly occupied by the mode localized at the right side with a phase difference of π, indicating that incident edge modes are switched to mode I.

By solving the ratio of the power of each eigenmode to the total power at the output terminal of the waveguide array through [34,35]

$$\eta = \frac{\left|\int \varphi^*(x)\psi(x)dx\right|^2}{\int \psi^*(x)\psi(x)dx \int \varphi^*(x)\varphi(x)dx}, \tag{6}$$

where φ and ψ stand for the distribution of the desired edge mode and the simulated output field at $z = L$ or 0, respectively, mode-transfer efficiencies above 98% can be obtained for all eight situations. To summarize, these results demonstrate an efficient asymmetric switching behavior of the edge-localized modes by dynamically encircling multiple EPs in a multistate system. In addition, it should be noted that the edge modes can be identified with both the intensity and phase distributions, which is significantly different from those in individual PT-symmetric and anti-PT-symmetric systems. The evolutions of edge modes in waveguide arrays with disturbed coupling coefficients caused by moving part of the waveguides along the x axis are also simulated and the calculated mode-transfer efficiencies are still close to 100%, according to the simulation results (see Sec. C in the Supplemental Material [57] for details), which indicates the robustness of the mode-switching characteristics of the system.

We also investigate the mode evolution in the waveguide array with $N = 3$ and $N = 4$. Structural parameters and refractive index distributions of the waveguide arrays are kept unchanged. It should be noted that as the number of waveguides increases, the propagation length needs to be increased to ensure a high mode-transfer efficiency. As a result, the waveguide length is set as $L = 3000$ μm for $N = 3$ and $L = 3400$ μm for $N = 4$, respectively. Figure 6 displays simulated distributions of E_y components at input and output terminals of the waveguide arrays (see Sec. B in the Supplemental Material [57] for the normalized $|\boldsymbol{E}|$ profiles). Similarly, the CW encirclement leads to a switching to edge mode IV, while the CCW encirclement leads to a switching to edge mode I, indicating that the asymmetric switching of the edge modes is still effective for the waveguide arrays as N increases. According to the electric field distributions of edge mode IV (I) and the outputs at $z = L$ (0), the calculated mode-transfer efficiencies are also close to 100%. Furthermore, the limited distribution range of the multiple EPs ensures that there are parameter loops that can encircle all the EPs even though the system tends to infinity. Therefore, the asymmetric switching of edge modes can be realized in more complex multistate systems by dynamically encircling an arbitrary number of EPs.

The mode switching discussed previously utilizes the spatial modulation of complex refractive indices. For practical applications, multiple methods can be used for achieving this purpose in waveguide array systems. For example, utilizing materials with variable refractive indices, such as liquid crystal [61] and lithium niobate [62], the refractive index modulation can be realized via the electro-optic effect. In addition, the variation of effective mode indices along the propagation direction can also be achieved by varying the sizes of the waveguides. The propagation loss and gain can be introduced by adding geometrical defects for enhanced scattering [63] and materials with light absorption or amplification [64] into the waveguide structures. Furthermore, the femtosecond-laser direct-writing techniques are also proved to be an effective method for fabricating waveguides with spatially variable effective mode indices [50]. These methods are highly desirable for the realization of mode switching in on-chip optical

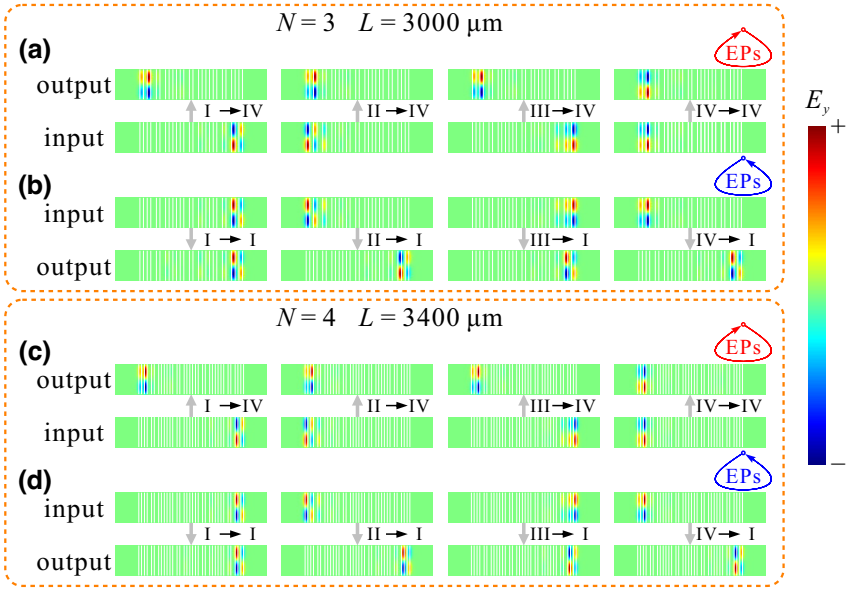

FIG. 6. Numerically simulated E_y profiles for (a),(b) $N = 3$ and (c),(d) $N = 4$ in both propagation directions. The corresponding $|\boldsymbol{E}|$ profiles are shown in Figs. S2 and S3 in the Supplemental Material.

systems and pave the way for further exploration on the experimental feasibility of this work.

V. CONCLUSION

In conclusion, an asymmetric switching of edge modes by encircling multiple EPs is demonstrated. A multistate non-Hermitian system is constructed based on a 1D lattice model, which supports multiple EPs in parameter space as well as four edge-localized modes. Dynamically encircling the EPs results in the specific edge mode possessing the largest gain surviving as the output, and this is determined by the encircling direction. Asymmetric switching of the edge modes through dynamically encircling multiple EPs is further demonstrated in optical waveguide arrays with refractive index modulation, in which CW (CCW) encirclement leads to an output mode localized at the left (right) side of the waveguide array with a phase difference of 0 (π), regardless of the input modes. Moreover, this effect can be extended to the multistate system with an arbitrary number of EPs. This work enables investigation of interesting effects in non-Hermitian physics by engineering the EPs and topological properties, especially for complex multistate systems. Furthermore, this work offers an alternative approach for switching the edge states of lattices, which will be useful for various nanophotonic devices, including mode convertors, optical switching, and routers.

ACKNOWLEDGMENTS

The authors acknowledge the support of the National Natural Science Foundation of China (Grants No. 11804109, No. 11974124, No. 12021004, No. 61975062) and Hubei Key Laboratory of Optical Information and Pattern Recognition, Wuhan Institute of Technology (Grant No. 202202).

[1] W. D. Heiss, The physics of exceptional points, J. Phys. A: Math. Theor. **45**, 444016 (2012).
[2] R. El-Ganainy, K. G. Makris, M. Khajavikhan, Z. H. Musslimani, S. Rotter, and D. N. Christodoulides, Non-Hermitian physics and PT symmetry, Nat. Phys. **14**, 11 (2018).
[3] M.-A. Miri and A. Alù, Exceptional points in optics and photonics, Science **363**, eaar7709 (2019).
[4] ŞK Özdemir, S. Rotter, F. Nori, and L. Yang, Parity-time symmetry and exceptional points in photonics, Nat. Mater. **18**, 783 (2019).
[5] M. Parto, Y. G. N. Liu, B. Bahari, M. Khajavikhan, and D. N. Christodoulides, Non-Hermitian and topological photonics: Optics at an exceptional point, Nanophotonics **10**, 403 (2021).
[6] E. J. Bergholtz, J. C. Budich, and F. K. Kunst, Exceptional topology of non-Hermitian systems, Rev. Mod. Phys. **93**, 015005 (2021).
[7] Q. Liao, C. Leblanc, J. Ren, F. Li, Y. Li, D. Solnyshkov, G. Malpuech, J. Yao, and H. Fu, Experimental Measurement of the Divergent Quantum Metric of an Exceptional Point, Phys. Rev. Lett. **127**, 107402 (2021).
[8] T. Goldzak, A. A. Mailybaev, and N. Moiseyev, Light Stops at Exceptional Points, Phys. Rev. Lett. **120**, 013901 (2018).
[9] C. Wang, X. Jiang, G. Zhao, M. Zhang, C. W. Hsu, B. Peng, A. D. Stone, L. Jiang, and L. Yang, Electromagnetically induced transparency at a chiral exceptional point, Nat. Phys. **16**, 334 (2020).
[10] H. Jing, ŞK Özdemir, Z. Geng, J. Zhang, X.-Y. Lü, B. Peng, L. Yang, and F. Nori, Optomechanically-induced transparency in parity-time-symmetric microresonators, Sci. Rep. **5**, 9663 (2015).

[11] H. Wang, W. Kong, P. Zhang, Z. Li, and D. Zhong, Coherent perfect absorption laser points in one-dimensional anti-parity-time-symmetric photonic crystals, Appl. Sci. **9**, 2738 (2019).
[12] C. Wang, R. Sweeney William, A. D. Stone, and L. Yang, Coherent perfect absorption at an exceptional point, Science **373**, 1261 (2021).
[13] S. Suwunnarat, Y. Tang, M. Reisner, F. Mortessagne, U. Kuhl, and T. Kottos, Non-linear coherent perfect absorption in the proximity of exceptional points, Commun. Phys. **5**, 5 (2022).
[14] S. Soleymani, Q. Zhong, M. Mokim, S. Rotter, R. El-Ganainy, and ŞK Özdemir, Chiral and degenerate perfect absorption on exceptional surfaces, Nat. Commun. **13**, 599 (2022).
[15] H. Ramezani, T. Kottos, R. El-Ganainy, and D. N. Christodoulides, Unidirectional nonlinear PT-symmetric optical structures, Phys. Rev. A **82**, 043803 (2010).
[16] X. Yin and X. Zhang, Unidirectional light propagation at exceptional points, Nat. Mater. **12**, 175 (2013).
[17] L. Feng, Y.-L. Xu, W. S. Fegadolli, M.-H. Lu, J. E. B. Oliveira, V. R. Almeida, Y.-F. Chen, and A. Scherer, Experimental demonstration of a unidirectional reflectionless parity-time metamaterial at optical frequencies, Nat. Mater. **12**, 108 (2013).
[18] Y. Huang, Y. Shen, C. Min, and G. Veronis, Switching of the direction of reflectionless light propagation at exceptional points in non-PT-symmetric structures using phase-change materials, Opt. Express **25**, 27283 (2017).
[19] Y. Huang, Y. Shen, C. Min, S. Fan, and G. Veronis, Unidirectional reflectionless light propagation at exceptional points, Nanophotonics **6**, 977 (2017).
[20] H. Hodaei, A. U. Hassan, S. Wittek, H. Garcia-Gracia, R. El-Ganainy, D. N. Christodoulides, and M. Khajavikhan, Enhanced sensitivity at higher-order exceptional points, Nature **548**, 187 (2017).
[21] T. Wu, W. Zhang, H. Zhang, S. Hou, G. Chen, R. Liu, C. Lu, J. Li, R. Wang, P. Duan, J. Li, B. Wang, L. Shi, J. Zi, and X. Zhang, Vector Exceptional Points with Strong Superchiral Fields, Phys. Rev. Lett. **124**, 083901 (2020).
[22] T. Xing, Z. Pan, Y. Tao, G. Xing, R. Wang, W. Liu, E. Xing, J. Rong, J. Tang, and J. Liu, Ultrahigh sensitivity stress sensing method near the exceptional point of parity-time symmetric systems, J. Phys. D: Appl. Phys. **53**, 205102 (2020).
[23] X.-G. Wang, G.-H. Guo, and J. Berakdar, Enhanced Sensitivity at Magnetic High-Order Exceptional Points and Topological Energy Transfer in Magnonic Planar Waveguides, Phys. Rev. Appl. **15**, 034050 (2021).
[24] H. Yang, X. Mao, G.-Q. Qin, M. Wang, H. Zhang, D. Ruan, and G.-L. Long, Scalable higher-order exceptional surface with passive resonators, Opt. Lett. **46**, 4025 (2021).
[25] W. Chen, Ş. Kaya Özdemir, G. Zhao, J. Wiersig, and L. Yang, Exceptional points enhance sensing in an optical microcavity, Nature **548**, 192 (2017).
[26] M. Liertzer, L. Ge, A. Cerjan, A. D. Stone, H. E. Türeci, and S. Rotter, Pump-Induced Exceptional Points in Lasers, Phys. Rev. Lett. **108**, 173901 (2012).
[27] M. Brandstetter, M. Liertzer, C. Deutsch, P. Klang, J. Schöberl, H. E. Türeci, G. Strasser, K. Unterrainer, and S. Rotter, Reversing the pump dependence of a laser at an exceptional point, Nat. Commun. **5**, 4034 (2014).
[28] B. Peng, ŞK Özdemir, S. Rotter, H. Yilmaz, M. Liertzer, F. Monifi, C. M. Bender, F. Nori, and L. Yang, Loss-induced suppression and revival of lasing, Science **346**, 328 (2014).
[29] H. Zhang, F. Saif, Y. Jiao, and H. Jing, Loss-induced transparency in optomechanics, Opt. Express **26**, 25199 (2018).
[30] J.-Q. Zhang, J.-X. Liu, H.-L. Zhang, Z.-R. Gong, S. Zhang, L.-L. Yan, S.-L. Su, H. Jing, and M. Feng, Topological optomechanical amplifier in synthetic PT-symmetry, Nanophotonics **11**, 1149 (2022).
[31] K. Kawabata, K. Shiozaki, M. Ueda, and M. Sato, Symmetry and Topology in Non-Hermitian Physics, Phys. Rev. X **9**, 041015 (2019).
[32] C. Dembowski, B. Dietz, H. D. Gräf, H. L. Harney, A. Heine, W. D. Heiss, and A. Richter, Encircling an exceptional point, Phys. Rev. E **69**, 056216 (2004).
[33] J. Doppler, A. A. Mailybaev, J. Böhm, U. Kuhl, A. Girschik, F. Libisch, T. J. Milburn, P. Rabl, N. Moiseyev, and S. Rotter, Dynamically encircling an exceptional point for asymmetric mode switching, Nature **537**, 76 (2016).
[34] X.-L. Zhang, S. Wang, B. Hou, and C. T. Chan, Dynamically Encircling Exceptional Points: *In situ* Control of Encircling Loops and the Role of the Starting Point, Phys. Rev. X **8**, 021066 (2018).
[35] X.-L. Zhang, T. Jiang, and C. T. Chan, Dynamically encircling an exceptional point in anti-parity-time symmetric systems: Asymmetric mode switching for symmetry-broken modes, Light: Sci. Appl. **8**, 88 (2019).
[36] W. Liu, Y. Wu, C.-K. Duan, X. Rong, and J. Du, Dynamically Encircling an Exceptional Point in a Real Quantum System, Phys. Rev. Lett. **126**, 170506 (2021).
[37] H. Qi, X. Hu, X. Wang, and Q. Gong, Encircling an exceptional point in a multiwaveguide anti-parity-time-symmetry system, Phys. Rev. A **103**, 063520 (2021).
[38] A. U. Hassan, B. Zhen, M. Soljačić, M. Khajavikhan, and D. N. Christodoulides, Dynamically Encircling Exceptional points: Exact Evolution and Polarization State Conversion, Phys. Rev. Lett. **118**, 093002 (2017).
[39] J. W. Yoon, Y. Choi, C. Hahn, G. Kim, S. H. Song, K.-Y. Yang, J. Y. Lee, Y. Kim, C. S. Lee, J. K. Shin, H.-S. Lee, and P. Berini, Time-asymmetric loop around an exceptional point over the full optical communications band, Nature **562**, 86 (2018).
[40] Q. Liu, S. Li, B. Wang, S. Ke, C. Qin, K. Wang, W. Liu, D. Gao, P. Berini, and P. Lu, Efficient Mode Transfer on a Compact Silicon Chip by Encircling Moving Exceptional Points, Phys. Rev. Lett. **124**, 153903 (2020).
[41] W. Liu, Y. Zhang, Z. Deng, J. Ye, K. Wang, B. Wang, D. Gao, and P. Lu, On-chip chiral mode switching by encircling an exceptional point in an anti-parity-time symmetric system, Laser Photonics Rev. **16**, 2100675 (2022).
[42] A. Roy, S. Jahani, Q. Guo, A. Dutt, S. Fan, M.-A. Miri, and A. Marandi, Nondissipative non-Hermitian dynamics and exceptional points in coupled optical parametric oscillators, Optica **8**, 415 (2021).
[43] J. Zhang, Z. Feng, and X. Sun, Realization of bound states in the continuum in anti-PT-symmetric optical systems: a proposal and analysis, Laser Photonics Rev. **17**, 2200079 (2023).

[44] H. Wang, S. Assawaworrarit, and S. Fan, Dynamics for encircling an exceptional point in a nonlinear non-Hermitian system, Opt. Lett. **44**, 638 (2019).
[45] S. Dey, A. Roy, and S. Ghosh, Light dynamics around an exceptional point in a 1D photonic bandgap waveguide, Phys. Scripta **97**, 085501 (2022).
[46] G. Elbaz, A. Pick, N. Moiseyev, and G. Shmuel, Encircling exceptional points of Bloch waves: Mode conversion and anomalous scattering, J. Phys. D: Appl. Phys. **55**, 235301 (2022).
[47] S.-Y. Lee, J.-W. Ryu, S. W. Kim, and Y. Chung, Geometric phase around multiple exceptional points, Phys. Rev. A **85**, 064103 (2012).
[48] K. Ding, G. Ma, M. Xiao, Z. Q. Zhang, and C. T. Chan, Emergence, Coalescence, and Topological Properties of Multiple Exceptional Points and Their Experimental Realization, Phys. Rev. X **6**, 021007 (2016).
[49] X.-L. Zhang and C. T. Chan, Dynamically encircling exceptional points in a three-mode waveguide system, Commun. Phys. **2**, 63 (2019).
[50] F. Yu, X.-L. Zhang, Z.-N. Tian, Q.-D. Chen, and H.-B. Sun, General Rules Governing the Dynamical Encircling of an Arbitrary Number of Exceptional Points, Phys. Rev. Lett. **127**, 253901 (2021).
[51] L. C. Lew Yan Voon and L. R. Ram-Mohan, Tight-binding representation of the optical matrix elements: Theory and applications, Phys. Rev. B **47**, 15500 (1993).
[52] S. Mao, A. Yamakage, and Y. Kuramoto, Tight-binding model for topological insulators: Analysis of helical surface modes over the whole Brillouin zone, Phys. Rev. B **84**, 115413 (2011).
[53] L. Feng, R. El-Ganainy, and L. Ge, Non-Hermitian photonics based on parity-time symmetry, Nat. Photonics **11**, 752 (2017).
[54] T. J. Milburn, J. Doppler, C. A. Holmes, S. Portolan, S. Rotter, and P. Rabl, General description of quasiadiabatic dynamical phenomena near exceptional points, Phys. Rev. A **92**, 052124 (2015).
[55] I. Gilary, A. A. Mailybaev, and N. Moiseyev, Time-asymmetric quantum-state-exchange mechanism, Phys. Rev. A **88**, 010102(R) (2013).
[56] E.-M. Graefe, A. A. Mailybaev, and N. Moiseyev, Breakdown of adiabatic transfer of light in waveguides in the presence of absorption, Phys. Rev. A **88**, 033842 (2013).
[57] See Supplemental Material at http://link.aps.org/supplemental/10.1103/PhysRevApplied.19.064050 for detailed analysis of the mode evolution processes (Sec. A), numerically simulated field profiles for $N=3$ and 4 (Sec. B), and effects of perturbation in coupling coefficients on mode switching (Sec. C).
[58] H. A. Haus and W. Huang, Coupled-mode theory, Proc. IEEE **79**, 1505 (1991).
[59] W.-P. Huang, Coupled-mode theory for optical waveguides: An overview, J. Opt. Soc. Am. A **11**, 963 (1994).
[60] A. Li, J. Dong, J. Wang, Z. Cheng, J. S. Ho, D. Zhang, J. Wen, X.-L. Zhang, C. T. Chan, A. Alù, C.-W. Qiu, and L. Chen, Hamiltonian Hopping for Efficient Chiral Mode Switching in Encircling Exceptional Points, Phys. Rev. Lett. **125**, 187403 (2020).
[61] C.-C. Shih, Voltage-controllable liquid crystal waveguide, Optik **127**, 2393 (2016).
[62] C. Wang, M. Zhang, X. Chen, M. Bertrand, A. Shams-Ansari, S. Chandrasekhar, P. Winzer, and M. Lončar, Integrated lithium niobate electro-optic modulators operating at CMOS-compatible voltages, Nature **562**, 101 (2018).
[63] S. Xia, D. Kaltsas, D. Song, I. Komis, J. Xu, A. Szameit, H. Buljan, K. G. Makris, and Z. Chen, Nonlinear tuning of PT symmetry and non-Hermitian topological states, Science **372**, 72 (2021).
[64] L. Feng, Z. J. Wong, R.-M. Ma, Y. Wang, and X. Zhang, Single-mode laser by parity-time symmetry breaking, Science **346**, 972 (2014).